Delft University of Technology

A six-degree-of-freedom micro-vibration acoustic isolator for low-temperature radiation detectors based on superconducting transition-edge sensors

Gottardi, L.; Van Weers, H.; Dercksen, J.; Akamatsu, H.; de Bruijn, M.P.; Gao, J. R.; Jackson, B.; Khosropanah, P.; Van Der Kuur, J.; Ravensberg, K.

Citation (APA)
Gottardi, L., Van Weers, H., Dercksen, J., Akamatsu, H., de Bruijn, M. P., Gao, J. R., Jackson, B., Khosropanah, P., Van Der Kuur, J., Ravensberg, K., & Ridder, M. L. (2019). A six-degree-of-freedom micro-vibration acoustic isolator for low-temperature radiation detectors based on superconducting transition-edge sensors. *Review of Scientific Instruments*, *90*(5), Article 055107. https://doi.org/10.1063/1.5088364

Important note
To cite this publication, please use the final published version (if applicable).
Please check the document version above.

A six-degree-of-freedom micro-vibration acoustic isolator for low-temperature radiation detectors based on superconducting transition-edge sensors

L. Gottardi, H. van Weers, J. Dercksen, H. Akamatsu, M. P. Bruijn (iD), J. R. Gao, B. Jackson, P. Khosropanah, J. van der Kuur, K. Ravensberg, and M. L. Ridder

View Online   Export Citation   CrossMark

ARTICLES YOU MAY BE INTERESTED IN

Scanning SQUID microscopy in a cryogen-free cooler
Review of Scientific Instruments **90**, 053702 (2019); https://doi.org/10.1063/1.5087060
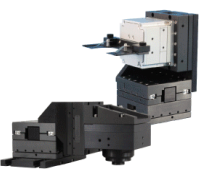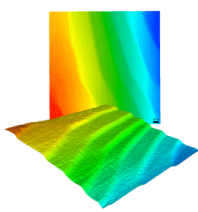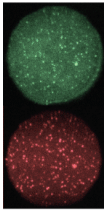
Vibration isolation with high thermal conductance for a cryogen-free dilution refrigerator
Review of Scientific Instruments **90**, 015112 (2019); https://doi.org/10.1063/1.5066618

Reactive power optimization of an active distribution network including a solid state transformer using a moth swarm algorithm
Journal of Renewable and Sustainable Energy **11**, 035501 (2019); https://doi.org/10.1063/1.5072789

Nanopositioning Systems

Modular Motion Control

AFM and NSOM Instruments

Single Molecule Microscopes

MCL MAD CITY LABS INC.
www.madcitylabs.com

AIP Publishing

A six-degree-of-freedom micro-vibration acoustic isolator for low-temperature radiation detectors based on superconducting transition-edge sensors

View Online   Export Citation   CrossMark

L. Gottardi,[1,a)] H. van Weers,[1] J. Dercksen,[1] H. Akamatsu,[1] M. P. Bruijn,[1] J. R. Gao,[1,2] B. Jackson,[3] P. Khosropanah,[1] J. van der Kuur,[3] K. Ravensberg,[1] and M. L. Ridder[1]

AFFILIATIONS

[1] SRON Netherlands Institute for Space Research, Sorbonnelaan 2, 3584 CA Utrecht, The Netherlands
[2] Faculty of Applied Sciences, Kavli Institute of NanoScience, Delft University of Technology, AQ2 9 Lorentzweg 1, 2628 CJ Delft, The Netherlands
[3] SRON Netherlands Institute for Space Research, Landleven 12, 9747 AD Groningen, The Netherlands

a)Electronic mail: l.gottardi@sron.nl

ABSTRACT

Dilution and adiabatic demagnetization refrigerators based on pulse tube cryocoolers are nowadays used in many low temperature physics experiments, such as atomic force and scanning tunneling microscopy, quantum computing, radiation detectors, and many others. A pulse tube refrigerator greatly simplifies the laboratory activities being a cryogen-free system. The major disadvantage of a pulse tube cooler is the high level of mechanical vibrations at the warm and cold interfaces that could substantially affect the performance of very sensitive cryogenic instruments. In this paper, we describe the performance of a very simple mechanical attenuation system used to eliminate the pulse-tube-induced low frequency noise of the superconducting transition-edge sensors under development for the instruments of the next generation of infra-red and X-ray space observatories.

https://doi.org/10.1063/1.5088364

I. INTRODUCTION

Superconducting transition-edge sensors (TESs) are very sensitive thermometers used in many low temperature applications. We are developing arrays of TES-based bolometers and microcalorimeters and the Frequency Domain Multiplexing (FDM) readout for the far-infrared SAFARI instrument on the Japanese mission SPICA[1] and for the X-ray Integrated Focal Unit (X-IFU) on board of the future X-ray observatory Athena.[2] A TES-based detector consists of a lithographically fabricated photon-absorbing structure coupled to a superconducting thin film with a sharp transition at its critical temperature T_C. The sensor is weakly linked to a thermal bath at a temperature lower than T_C and is kept at a working point between the superconducting and normal state by a constant or ac voltage. Depending on the magnitude of the thermal link and the absorber

typology, such a device operates as a power detector, very sensitive, for example, to far-infrared radiation, or as a single photon detector with very high resolving power for X-ray or gamma-ray spectrometry. The thermal link to the bath is realized by means of a few millimeter-long and submicrometer-thin SiN beams, in the case of the bolometers, or a micrometer-thin SiN membrane, in the case of the X-ray detectors. Very high power sensitivity has been achieved with TES-bolometers fabricated at SRON, with a demonstrated Noise Equivalent Power (NEP) of $< 2 \times 10^{-19}$ W/$\sqrt{\text{Hz}}$ under ac-bias.[3,4] TES microcalorimeters under development for X-IFU have a typical energy resolution lower than 2 eV for a photon energy of 6 keV and measured in a single pixel dc-bias readout mode.[5] An energy resolution of 2.6 eV at 6 keV has been demonstrated at SRON with the NASA-Goddard X-ray detectors measured in this work at MHz bias.[6] Energy resolution below 2 eV has been recently

reported under MHz biasing with devices of new generation.[7] From the mechanical point of view, a TES's array is a mass-spring system potentially sensitive to microvibrations transmitted through its supporting structures. Mechanical dissipations nearby the detectors could generate temperature or power fluctuations and deteriorate their sensitivity.

The TES-based detectors described in this paper have a T_C of about 100 mK and operate at a typical bath temperature of 50 mK, which is achieved with Dilution Refrigerators (DR) or Adiabatic Demagnetization Refrigerators (ADR). In both cases, the lower temperature stages are precooled by a Pulse Tube (PT) cryocooler with one cold head with two stages, at 50 K and 3 K, respectively.[8] The cooling mechanism of a PT is based on compression and expansion of He^4 gas through an orifice. High pressure pulses are generated in the PT at a typical driven frequency of few hertz, and the gas pressure oscillates between 5 and 20 bars. The gas pulses are squared wave-like with harmonics measurable up to 20 kHz.[9,10] Their intensity is large enough to produce acoustic vibrations in a wide frequency range that easily propagate to the 50 mK stage and the experimental setup. Furthermore, the room temperature mechanical compressor and the rotary valve used to drive the gas in the pulse tube generate mechanical vibration at the top flange of the cryostat.

Performance deterioration of low temperature detectors, caused by PT-induced mechanical vibrations, has been reported in many different fields, such as, for example, in gravitational wave detector experiments,[11] in atomic resolution scanning tunneling microscopy,[12] in dark matter search detectors,[13] and in qubit devices.[14] The coupling mechanism between the mechanical vibrations and the detector could be different for different applications. In the scanning tunneling atomic microscope, for example, mechanical vibrations at low frequencies generate excess displacement noise in the setup,[12] while in the qubit experiments, acoustic oscillations can contribute to dephasing through motion in an inhomogeneous magnetic field or microphonic effect on the readout lines.[14]

In this paper, we will report on the performance of a six-degree-of-freedom passive mechanical vibration attenuation developed to eliminate the mechanically induced fluctuations in ultralow noise TES-based bolometer detectors and high resolving power TES-based microcalorimeters. The vibration isolator is a multistage mass-spring system designed to be most effective at the kilohertz frequencies.

II. EXPERIMENTAL SETUP

For the experiments described in this paper, we use a cryogen-free DR from Leiden Cryogenics precooled to 3 K by a two-stage Cryomech PT-415 pulse tube cryocooler, which is driven by a CP1000 helium compressor. The motor-head rotary valve, which connects alternatively the high and low pressure lines of the compressor at a rate of about 1.5 Hz, is electrically decoupled from the main body of the cryostat. The mechanical connection to the PT-head is done by means of a "swan-neck" shaped motor-head flex-line. We use a linear driver to control the rotary valve as it has been proven to reduce the vibration at the upper stage of the cryostat. The pulse tube is hard connected to the 50 K and 3 K plates. A schematic of the cryogen-free DR, including the pulse tube and the experimental setups, is shown in Fig. 1. At the top flange of the cryostat, we have mounted a loudspeaker to mechanically excite the cryostat

resonant modes in a frequency range from 40 to 2000 Hz. The cryostat has been modified to provide high electromagnetic interference (EMI) rejection at the location of the experimental setups and consists effectively in two nested Faraday cages.

Three FDM setups, called here below *bolo-FDM*, *X-FDM*, and *FDM-probe*, have been used to probe the vibration level at the 30 mK stage. They all consist of arrays of TES-based detectors readout with the FDM setups under development for the infrared and X-ray instruments SAFARI[15] and X-IFU.[6] More details on the FDM setups are reported in the Appendix. In the X-ray FDM experiments, mechanical vibrations could be responsible for the measured low frequency noise and the reported stability issue of the spectrometer.[6] The bolometer FDM setup is the one most susceptible to mechanical vibration. As a matter of fact, all the results reported so far with these detectors, showing electrical Noise Equivalent Power (NEP) as low as 1×10^{-19} W/$\sqrt{Hz}$,[3,4] have been obtained by switching off the pulse tube during the noise spectra acquisition.

III. PULSE TUBE NOISE AND THE VIBRATION ISOLATION SYSTEM

We estimate the effect of the pulse tube on the vibration of the mixing chamber plate by measuring at room temperature the horizontal and vertical acceleration with a Bruel and Kjaer 8306, uniaxial accelerometer, placed on the mixing chamber plate at the position of the X-ray FDM setup. The accelerometer is sensitive from 0.3 Hz to few kHz and calibrated from 0.3 to 1000 Hz. In Fig. 2, we show the acceleration spectral density (ASD) taken in both the vertical (Z) and horizontal (X) directions with the PT switched on and off, respectively. When the PT is operational, at frequencies below 20 Hz, the vibrational peaks at the PT modulation frequency are clearly visible up to the tenth harmonics and more. The acceleration noise at the peaks increases of about two orders of magnitude with respect to the background fluctuations. The rms displacement noise in the frequency range below 20 Hz calculated from the displacement spectral density $DSD = ASD/(2\pi f)^2$ is 12.5 μm and 7.2 μm in the horizontal and vertical direction, respectively. These values should be compared with the noise measured with the PT off, equal to 8.1 μm and 5.4 μm, respectively. The acceleration noise at frequency above 100 Hz is significantly higher when the PT is switched on. Peak noise values of the order of $\sim 5 \times 10^{-5}$ g/$\sqrt{Hz}$, with $g = 9.806\ 65$ m/s^2, were observed in both directions in the kilohertz range. When the PT is off, the acceleration noise values around 1 kHz are generally well below 10^{-6} g/$\sqrt{Hz}$. These values correspond to an rms displacement noise in the frequency bandwidth between 700 Hz and 1.6 kHz of 24 pm and 18 pm with the PT on for the X and Z direction, respectively, and of ~1.1 pm in both directions with the PT off.

TES-based detectors are relatively insensitive to direct mechanical displacement when they are properly shielded from residual magnetic fields. Being thermal detectors, they are of course very sensitive to the power dissipated directly in the pixel, in the SiN suspending membrane/legs, in the Si chip, or in the copper bracket. The average dissipated power, due to an input acceleration noise of the test mass, in the case of a single suspended mass m, structural low damping, and a white-noise input spectrum, is, in first approximation, independent of the suspension's resonance frequency and the
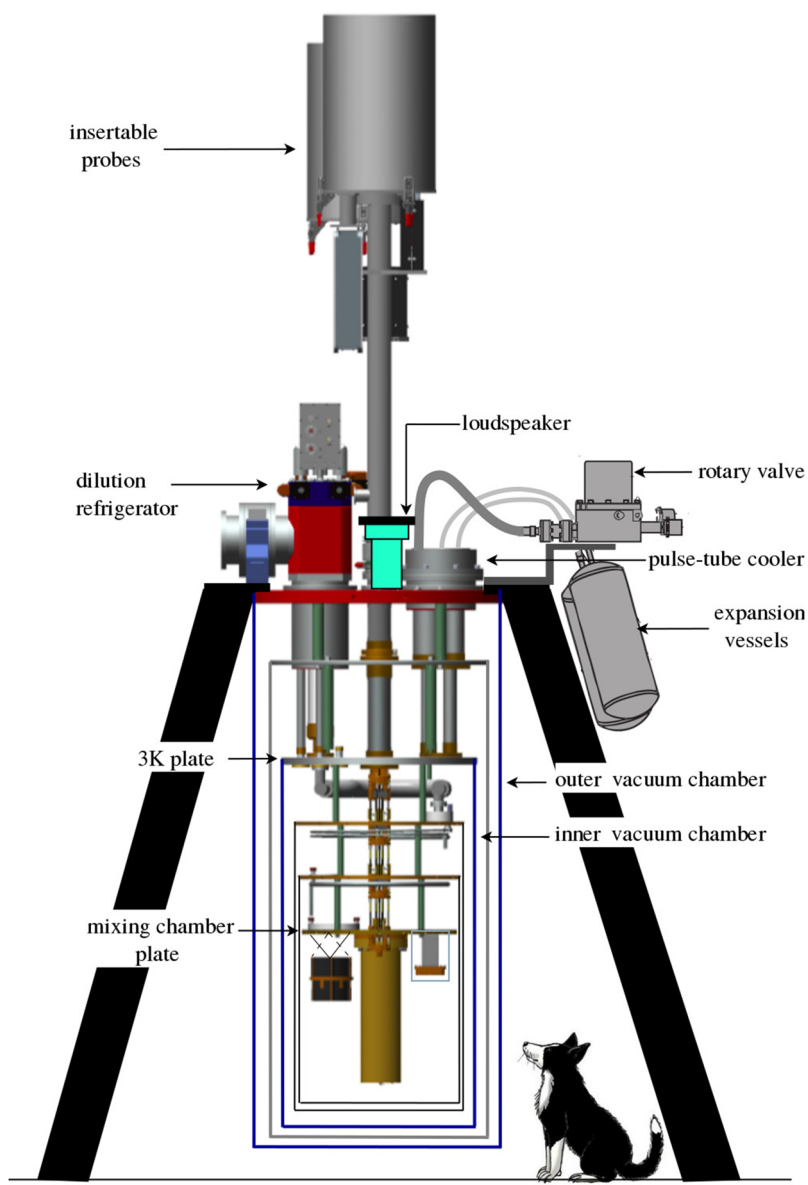
FIG. 1. The cryogen-free DR from Leiden Cryogenics pre-cooled to 3 K by a two-stage Cryomech PT-415 pulse tube and hosting several FDM setups. A loud speaker at the top of the cryostat allows us to excite the acoustic modes of the cryostat from 40 to 2000 Hz. Two 50-mm top-loading probes, mounting other experimental setups, can be inserted through a clear shot. The whole cryostat, including the probes, has been modified to be EMI tight following a nested Faraday cage concept.

damping coefficient. It can be shown to be $P_{diss} \simeq m S_a/8$ when integrated over the frequency range around the resonance.[16] Here, m is the mass of the accelerated body and $\sqrt{S_a}$ is the ASD in units of $m/s^2/\sqrt{Hz}$. The temperature fluctuations associated with the dissipated power are given by $\delta T = P_{diss}/G$, where G is the thermal conductivity of the accelerated mass to the thermal bath. A realistic calculation of the dissipated power is complicated and requires the definition of a multi-degree-of-freedom mass-spring model and a finite element analysis of a complicated structure.[16] The simple single mass-spring model can be used though to derive the order of magnitude of the dissipation. As an example, the TES bilayer thin film and the SiN island have a total calculated mass of $m \sim 14.4 \times 10^{-12}$ kg. The resonant frequency of the vibrational

modes of the mass-spring system, consisting of the bolometer island and the 4 legs, has been estimated to be about few kilohertz. An input acceleration noise of $\sqrt{S_a} \sim 4 \times 10^{-5}$ g$/\sqrt{Hz}$, comparable to the one measured around 1 kHz on the mixing chamber plate with the PT active, as shown in Fig. 2, would dissipate in the legs-detector system, an averaged rms power of about 3×10^{-19} W. This is about a factor of 2 higher than the power that the TES bolometer under test can typically detect at low frequencies in a 1 Hz bandwidth. A similar calculation, using this time the mass of the detectors array Si chip, estimated to be $m \sim 8.4 \times 10^{-5}$ kg, gives an average dissipated rms power into the chip of about 2 pW at few kilohertz. Given the nominal value of the thermal conductance of a Si wafer at 50 mK, $G \sim 100$ nW/K, this corresponds to fluctuations of the Si chip temperature of the
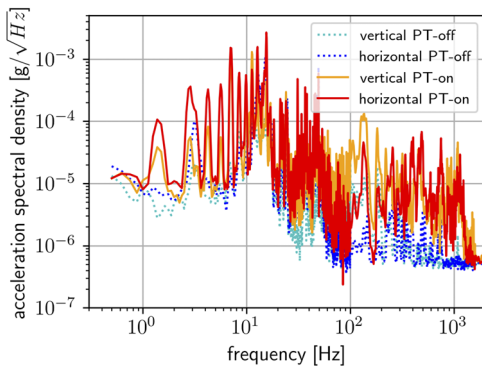
FIG. 2. Vertical, *Z*, and horizontal, *X*, acceleration spectral density, measured at room temperature with an accelerometer mounted on the mixing chamber at the position of the X-ray FDM setup. The *g* in the units is the gravitational acceleration $g = 9.806\ 65\ m/s^2$. The spectra are taken both with the PT switched on and off.

FIG. 3. Spectrogram of the TES bolometer P23 signal showing the evolution in time of the current spectral density between 70 and 4000 Hz. (a) TES in transition and (b) TES in the normal state. Note the difference in color scale.

order of $dT_{rms} \sim 20\ \mu$K. Even larger dissipations may occur in the bracket and the mechanical structures holding the detectors. This is due to the larger mass of those structures (in the order of hundreds of grams), and their lower frequencies vibrational modes. These not-negligible power dissipations could explain the large observed TES bolometer current fluctuations reported in Fig. 8.

In Fig. 3, we plot a spectrogram of the bolometer P23 signal showing the evolution of the power spectral density (PSD) in time. Each spectrum is calculated from a 30 ms time record and shows the detector PSD from 70 Hz to 4000 Hz. When the bolometer detector is thermally active, the low frequency noise ($f < 200$ Hz) correlates with the 1.4 Hz PT beat occurring at ~0.5, 1.2, 1.9, and 2.6 s in the data set of Fig. 3(a). No excess noise is observed when the detector is in the normal state [Fig. 3(b)].

The current spectral density of a single pixel of the FDM bolometer and of the X-ray FDM setup was measured during the normal operation of the cryocooler and with the PT temporarily switched off. In both cases, the pixels were biased in the transition at their most sensitive bias points. The TES's noise spectra are reported in Fig. 4. The TES calorimeter shows a clear signature of the PT switching rate and its harmonics on top of an excess low frequency noise. The low frequency noise tail is caused by the room temperature electronics used in this particular experiment and is not directly related to the PT activity. In the bolometer case, the excess noise at low frequencies, induced by the pulse tube, is several orders of magnitude higher than the detector intrinsic noise and extends up to hundreds of hertz. The excess noise completely disappears when the PT is temporarily switched off.

We believe that the observed low frequency fluctuations are caused by the modulation of the power dissipated locally by mechanical vibration of the structures supporting the detector pixels. These structures include the thermally regulated copper bracket, where the array chip is mounted, the silicon chip itself, the Si beams, and the SiN long legs or the membrane of the TES themselves. The vibrational modes of these mechanical components are typically in the frequency range from 50 Hz up to several kilohertz. A low-frequency modulation of these resonant modes, either with white-noise or coherent input spectrum, would induce a low frequency modulation
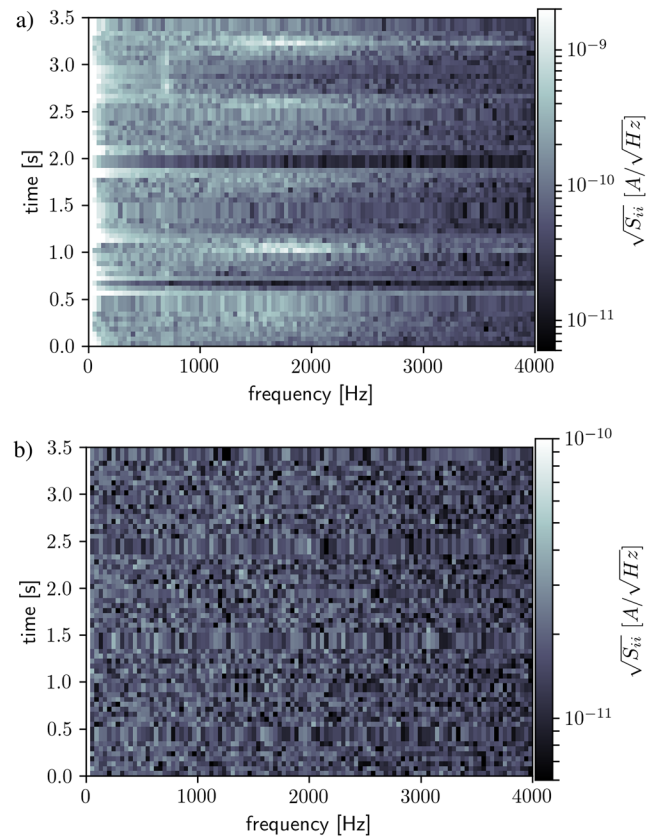
of the power dissipated in the modes. This could lead to a low frequency fluctuation of the operating temperature or a direct power noise in the sensitive detector. The eigenfrequencies of the detector pixels supporting legs or membrane are expected to lie in the kilohertz range, well above the PT operating frequencies. In this regard, the pulse tube can be seen as a hammer, generating strokes at 1.4 Hz and higher harmonics. These low-frequency excitations could be then upconverted to high frequency via nonlinear processes occurring in the complex mechanical assembly of the cooler, resulting in the vibrational spectra observed in Fig. 2. The high frequency vibration noise could couple to the detector silicon structures and cause thermal and power fluctuations. A useful experiment to discriminate whether the fluctuation is caused by bath temperature or detector power fluctuation is to perform the low frequency noise measurement at higher bath temperatures at which the TES detectors become very sensitive. Preliminary tests have not given a conclusive answer yet, and further investigation is ongoing.

The other dissipation mechanism related to microvibrations could be originated, for example, from spurious magnetic coupling or from microphonics in the cryoharness and the FDM superconducting circuit. We can investigate these mechanisms by working with the TES's in the normal and superconducting states. The
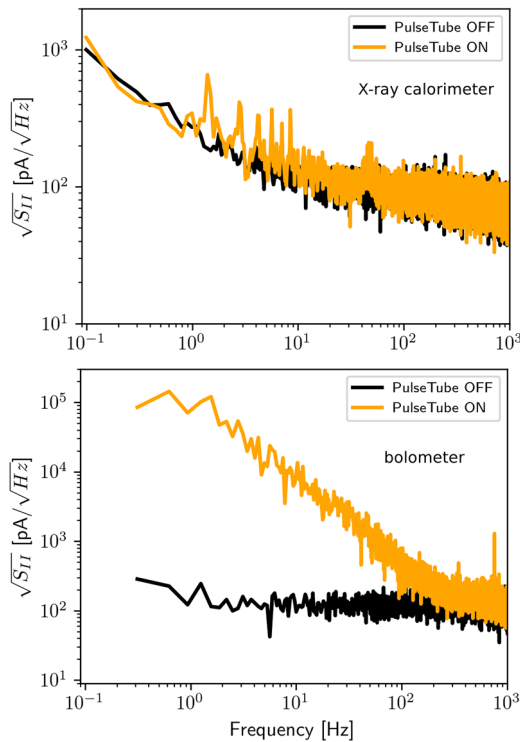
FIG. 4. Current spectral density of a single pixel from the FDM bolometer (*lower*) and from the X-ray FDM array (*upper*). The data were taken with the pixels biased at their most sensitive operating point, during the normal operation of the cryocooler, and with the PT temporarily switched off. The low frequency noise tail in the *upper* plot is caused by the room temperature electronics used in this particular experiment and is not related to the mechanical vibration.
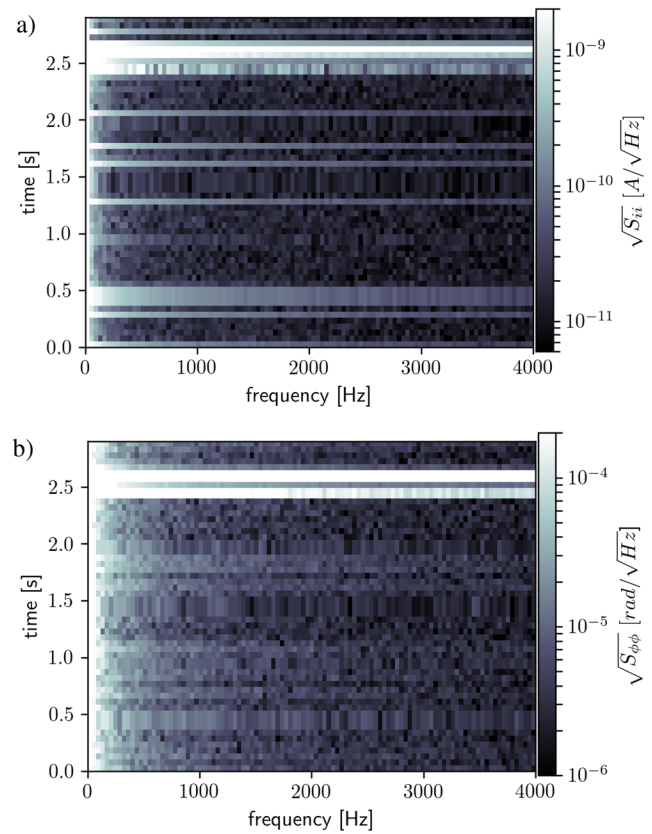

FIG. 5. Evolution in time of current amplitude (a) and phase (b) spectral density of pixel P23 in the superconducting state.

forward path of the Superconducting QUantum Interference Device (SQUID) readout signal has been proven to be insensitive to the PT activity. The test was done by biasing the TES in the normal state and taking noise spectra in time. By operating the TES in the normal state, we increase the impedance of the SQUID input circuit such that the intrinsic noise of the SQUID and the room-temperature electronics can be observed. The spectrogram of the SQUID output amplitude, taken with pixel P23 in the normal state, is shown in Fig. 3(b). The noise is white down to low frequency and no correlation with the cooler pulse rate is observed when the detector is in the normal state.

A similar test was done with the TES in the superconducting state. In this case, the noise at low frequencies is fully dominated by the Johnson noise of the high-Q LC filters and the ac bias circuit. With the TES's in the superconducting state, the system is more susceptible to microphonics and impedance changes, for example, in the ac bias line or in the LC resonant loop. Instabilities in the bias signal lead to excess fluctuations in the current measured by the SQUID amplifier. The spectrogram in Fig. 5, taken with pixel P23 in the superconducting state, is a measurement of the evolution in time of the current noise of the superconducting circuit. A weak correlation with the PT beats has been observed. Excess noise at low frequencies and sudden jumps in the baseline are detected

regularly, but not always in correlation with the PT beats. Instabilities related to the high-Q readout circuit or the ac bias signal is better detected by monitoring the phase between the megahertz carrier and the output signal [Fig. 5(b)]. The phase noise is white at high frequencies and increases at frequencies below 200 Hz. As in the current amplitude spectrogram, the phase occasionally shows jumps in the baseline. Noise induced by the mechanical displacement of the detector and the readout circuit in a nonuniform magnetic field, or microphonics in the harness, could be the cause of the fluctuations observed in Fig. 5. For example, the modulation of the total inductance of the resonant circuit, caused by displacement in a nonuniform magnetic field, would change the working point of the TES in transition and could be responsible for the observed fluctuation when the TES is thermally active. The bolometer FDM bracket was shielded by a superconducting Nb shield only, and no cryoperm or μ-metal shields was used in the experiments presented here. The residual perpendicular DC magnetic field in the detector array area has been zeroed using the Helmholtz coil[17] available on the FDM setup. When we operate the TES in transition and change the applied perpendicular magnetic field at the array side, we do not observe significant difference in the current fluctuation level. This indicates that if the displacement in the magnetic field was responsible for the excess noise, then the effect should occur in the FDM bias

and readout circuit rather than at the detector side. As a matter of fact, the LC filters and the other components of the readout circuit were exposed to the residual nonuniform magnetic field consisting mainly of the sum of the Earth magnetic field and the external field generated by the Helmholtz coil. This is however unlikely, given the fact that all the coils in the SQUID amplifier and the LC filters have a gradiometric design, which make them insensitive, in the first order, to the magnetic field.

The amplitude of the high frequency mechanical vibrations can be greatly reduced by implementing a vibration attenuation stage between the detector setup and the cold stage of the DR. An optimized vibration isolation system needs to provide sufficient attenuation in all six degrees of freedom and in the frequency range where the largest mechanical coupling to the experiment is expected. Two other important requirements, specific for the low temperature applications, are that it must generate low thermal dissipations and guarantee sufficient thermalization to the DR 30 mK stage. Passive mass-spring systems can be very effective in suppressing vibrations at audio frequencies, as demonstrated, for example, in the low temperature gravitational wave resonant detectors.[18–23]

A single stage mechanical passive filter consists of a resonator of mass m and spring constant k with a natural resonant frequency $\omega_o = \sqrt{k/m}$ lower than the frequency ω to be filtered. The transfer function of a low-loss system for one degree of freedom at $\omega \gg \omega_0$ is given by

$$T(\omega) = \frac{\omega_0^2}{\omega^2 - \omega_0^2}. \qquad (1)$$

Attenuation of four orders of magnitude could be ideally achieved at two decades above the natural frequency of the filter. In the case of a n-stage mass-spring system with identical mass and natural resonant frequencies, the displacement attenuation from the support to the nth suspended mass is given by $(\omega_0/\omega)^{2n}$. A multistage passive isolation system can be very effective at frequency well above the single stage natural frequency. At high frequencies however, both the spring and the mass do not behave as ideal elements any more, due to their internal modes of vibrations. With a careful design of the elements and a proper selection of the materials, it is possible to move the internal resonances at frequencies higher than the ones at which the suspensions have to be effective. It can be shown[20] that the natural frequency of a mass-spring system is proportional to $\sqrt{E\rho}/\sigma_{max}$, where E is the Young's module, ρ is the mass-density and σ_{max} is the yield strength. The material of the elastic element should then have low density, high yield strength, and a low Young's modulus to lower the suspension frequency with a large payload mass.

The disadvantage of a passive mass-spring mechanical filter is that it is effectively an oscillator at low frequencies. In general, the mechanical vibrations are not attenuated below the resonance frequency of the filter and can become significantly large at resonance when they are not sufficiently damped. For this reason, it is very critical to choose spring materials which minimize the Q-factor of the isolator pendulum modes. We developed a vibration isolation system similar to the one described by Chan *et al.*[19] It consists of a vertical stack of masses connected by tensioned straight wires that act as springs. A schematic of the suspension structure is shown in Fig. 6. The wire triangular configuration provides bending stiffness and comparable attenuation in all the six degrees of freedom.
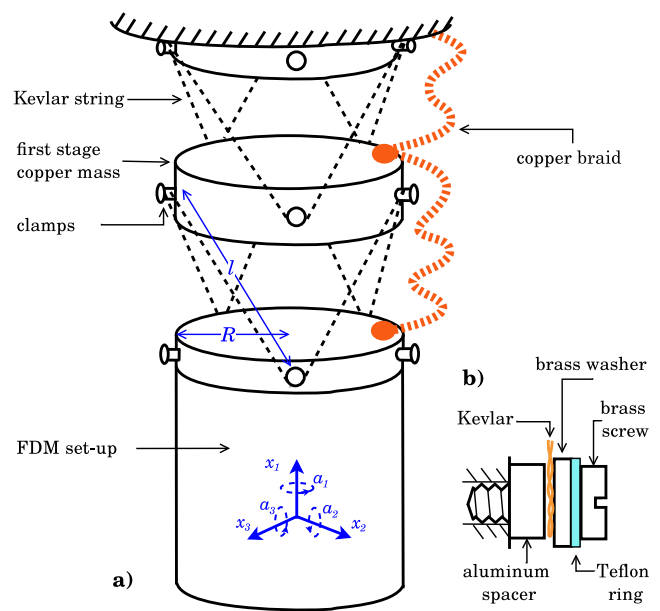

FIG. 6. (a) Schematic drawing of the two-stage mechanical attenuator developed to reduce microvibration induced noise in the TES bolometers array. Two copper disks of identical diameter have been rigidly mounted on the bottom part of the dilution cooler mixing chamber plate and on the top part of the FDM setup to be suspended. An intermediate copper mass has been used as an intermediate stage. A Kevlar string of total length of 6l, clamped to the side of the masses as shown in detail in (b), has been used to suspend each mass. The wire triangular configuration provides bending stiffness and comparable attenuation in all the six degrees of freedom.

The lowest transverse frequency of a wire under tension is equal to $\omega_s = \pi/l\sqrt{\sigma_{max}/\rho}$, with l being the wire length. Consequently, by choosing a material with high yield strength and low density, the intrinsic resonances of the spring can be moved toward high frequencies. Kevlar is the ideal material for this application thanks to the very high longitudinal yield strength, its low mass density, a low Young's module with respect to any metal wires, and its compatibility with vacuum and cryogenic applications. Kevlar cords have a stiffness to thermal conductivity ratio 10 times larger than stainless steel cables. They have been used, for this reason, in many experiments at temperatures below 1 K to combine high thermal isolation and mechanical rigidity.[24]

We have tested the X-ray FDM setup with a single-stage mechanical isolator and the bolometer FDM setup with a single-stage and a two-stage isolator, as schematically shown in Fig. 6. Two copper disks of identical diameter have been rigidly mounted on the bottom part of the dilution cooler mixing chamber plate and on the top part of the FDM setup to be suspended. An intermediate copper mass, of the same diameter as the FDM setup, has been used in the two-stage configuration experiment. A Kevlar string of diameter d and a total length of 6l has been used to suspend each mass. The two ends of the Kevlar wire are connected together with *Fisherman's knot* to form a closed ring, which is used to hang the stage below. The Kevlar wires are firmly connected to the disks by means of clamps, as shown in Fig. 6(b). On the side of the copper disks, six

holes have been symmetrically drilled every 60° to host the Kevlar wire clamps. The latter consist of a brass screw inserted into an aluminum spacer, a brass washer, and a Teflon ring, as shown in detail in Fig. 6. The aluminum spacer is needed to prevent that the Kevlar wires touch the upper edge of the copper disk. The Kevlar wire is clamped between the aluminum spacer and the brass washer when the brass screw is fixed into the side holes of the stage disks. The Teflon ring is used to minimize the rotation of the brass washer during clamping. Before tightening the screws, the Kevlar-disk system was adjusted to get equal length on each segment of the wire and to ensure uniform wire tension provided by the weight of the hanging stage. The total mass of the final spring-mass stage was given by the FDM setup itself and the copper disk connected to it. The thermalization of the FDM setup is achieved by means of soft copper braids, sufficiently long to prevent a mechanical short of the Kevlar springs.

A simple analytical lumped-element model was used to dimension the vibration isolation system following the work of Chan et al.[19] The dimension of the damping system and the parameters used in the model are given in Table I. The Kevlar wire length and thickness have been chosen to get the natural frequencies around 100 Hz or below. In Fig. 7, we show the calculated transfer functions for the three transversal and three rotational vibration modes of the bolometer FDM setup for the single (a) and the two-stage (b) configuration.

The lumped elements model predicts the pendulum modes to be lower than 100 Hz for the single-stage system and lower than

TABLE I. Physical parameters of the two-stage spring-mass vibration isolation system used in the bolometer FDM setup and formulas of the natural frequencies used to calculate the damping factor in all the six degrees of freedom. The equations are derived in Chan et al. paper[19] and references therein.

| Parameter	Value
Spring	
Material	Kevlar
Length per stage, l	80 (mm)
Diameter, w_s	200 (μm)
Cross section, $A = \pi w_s^2/4$	3×10^{-8} (m^2)
Density, ρ_k	1470 (kg/m^3)
Yield strength, σ_{max}	2.49×10^9 (N/m^2)
Young's modulus, E	1.12×10^{11} (N/m^2)
Mass	
Mass 1, m_1	1.5 (kg)
Mass 2, m_2 (incl. FDM setup)	3.5 (kg)
Radius, R	50 (mm)
Height of mass 1, H_1	20 (mm)
Height of mass 2, H_2	120 (mm)
Natural frequencies	
Translational x_2 and x_3	$\omega_{x2,x3} = R\sqrt{\dfrac{3EA}{m_{1,2}l^3}}$
Translational x_1	$\omega_{x1} = \sqrt{\dfrac{6EA(l^2-R^2)}{m_{1,2}l^3}}$
Rotational α_2 and α_3	$\omega_{\alpha_2,\alpha_3} = 2\sqrt{\dfrac{6EA(l^2-R^2)}{m_{1,2}l^3\left(1+\frac{1}{3}\left(\frac{H}{R}\right)^2\right)}}$
Rotational α_1	$\omega_{\alpha_1} = 3R\sqrt{\dfrac{EA}{m_{1,2}l^3}}$
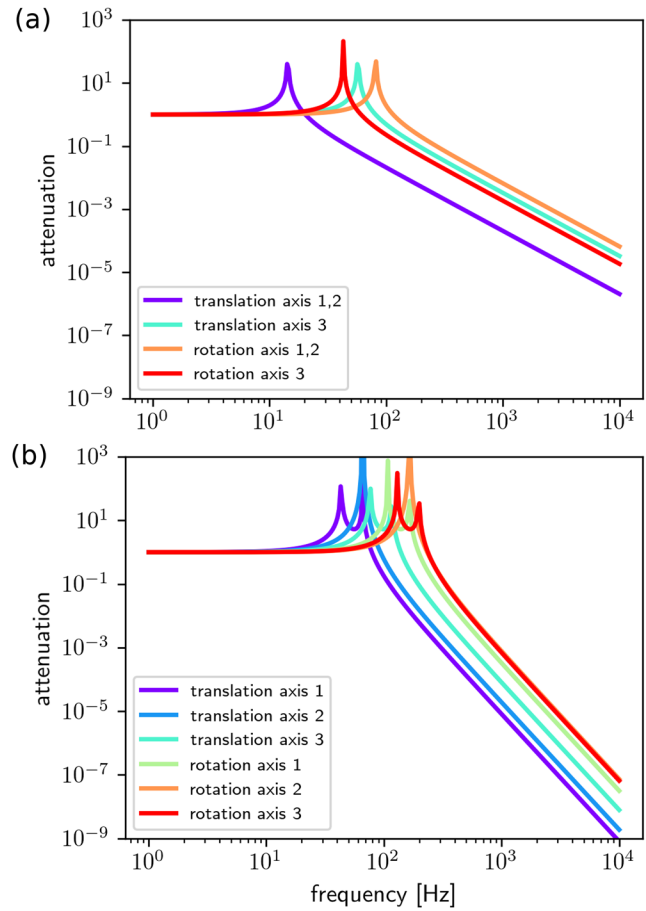
FIG. 7. Attenuation of the three transversal and three rotational vibration modes calculated using a lumped element model of the bolometer FDM setup in the single (a) and in the two-stage (b) configuration.

200 Hz for the two-stage system. No dissipation mechanism has been included in the model. In the real system, we expect the Q-factor and the peak value of the pendulum modes to be lower than the calculated one due to the losses in the Kevlar string and at the clamping points. In the kilohertz range, we expect to reach an attenuation level of 10^{-3} and 10^{-5} with the single and two-stage attenuation systems, respectively.

IV. EXPERIMENTAL RESULTS

We have done the following experiment to identify which vibrational modes of the cooler and the detector assembly affect the TES response. Using a loudspeaker on top of the cryostat, we excite the vibrational modes of the system by slowly scanning the frequency from 40 to 2000 Hz. Simultaneously, we recorded the multiplexed signal from several pixels of the three FDM setup described above. All the pixels were biased at their superconducting transition. No temperature controller has been used during this measurement, and the base temperature of the FDM brackets was freely drifting and fluctuating around 50 mK. In this way, we could monitor

directly, during the frequency sweep, the bath temperature of all the three setups. In Fig. 8, we plot the pixels baseline and the bracket temperature as a function of the excitation frequency for the bolo- and X-FDM setups, respectively. The signal from the bolometers is very noisy as a consequence of the vibrations induced by the PT. At very specific frequencies, the detector is thermally excited up to a level that the pixels become normal and the signal drops dramatically. At this point, the detector is not sensitive any more. The X-ray calorimeters are less sensitive to the vibration as it can be seen in the tracks of Fig. 8(b). A similar data set for the FDM-probe is shown in Fig. 9. In this case, the measurements were done in two cryogenic runs, and the second one performed after rotating the probe mechanical clamping position of 90°.

FIG. 9. Baseline signal of four TES's of the X-FDM probe as a function of the excitation frequency of the vibration induced by the loudspeaker at the top of the cryostat. The probe was clamped to the hole in the mixing chamber plate in two orthogonal positions (a) and (b) as described in the schematic diagram at the bottom-right of the plots. In (b), the bath temperature variation during the frequency scan is shown as a black line.
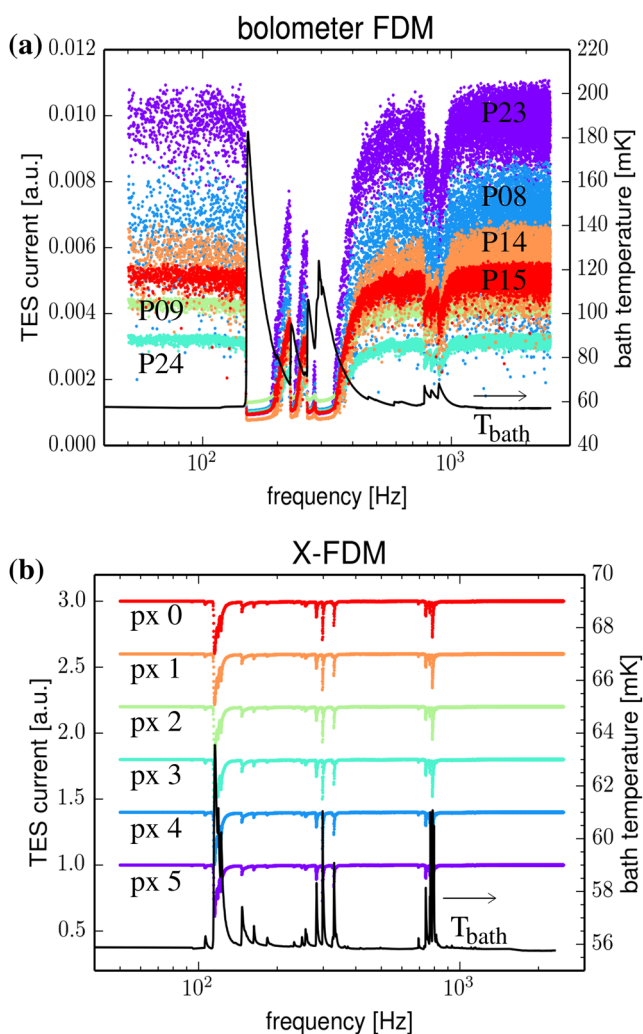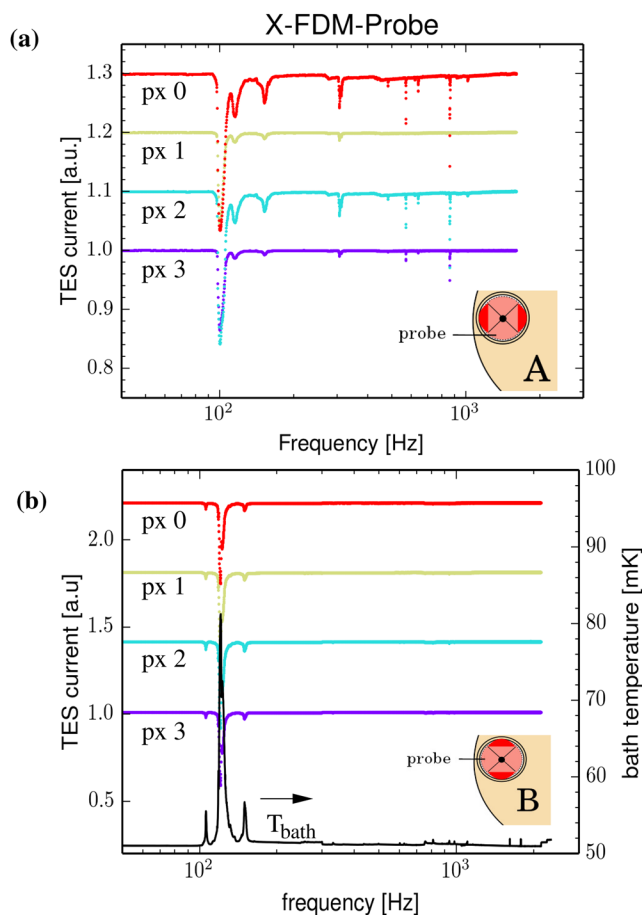

FIG. 8. Baseline signal of the six TESs of the FDM bolometer setup (a) and the X-FDM setup (b) as a function of the excitation frequency of the vibration induced by the loudspeaker at the top of the cryostat. The black curve shows the bath temperature variation during the frequency scan. Both setups are directly connected to the mixing chamber plate of the dilution refrigerator.

In all the FDM experiments, we observe three main groups of resonances, namely, at about 120, 300, and 800 Hz. There are resonance frequencies which are common to all the three setups and others which are specific to the single FDM setup. This is the case, for example, for the modes at 100 and 120 Hz, which are observed in the X-ray detectors, but not in the bolometer experiment, or the mode at 220 Hz observed with the bolo-FDM and not with the X-FDM and the FDM-probe. The change in the TES detector signal correlates with the temperature of the copper bracket. This indicates that the vibrational modes of the FDM mechanical assembly dissipate heat in the bracket that cause fluctuation of the bath temperature and in the detector response. The fact that all pixels of one FDM setup react in the same way to the acoustic excitation is consistent with the observation above. The frequency peaks in common with all the three setups are very likely generated by the resonant mode of the DR mixing chamber plate and other mechanical structures of the cooler. This is the case, for example, of the modes at

around 300 Hz. By looking at Fig. 9, it is interesting to notice that, in the probe, the response to mechanical excitations depends on the orientation of the mechanical clamps in the hosting hole of the mixing chamber. As an example, the 300 Hz vibrational modes dissipate power in the FDM-probe when the insert is clamped in position A, as shown in Fig. 9(a), and baseline fluctuations are observed at these frequencies. When the probe is clamped in position B, rotated 90° with respect to position A, the level of the vibrations at 300 Hz is below the signal resolution, as shown in Fig. 9(b).

Under normal operation, the bath temperature of the FDM experiments is stabilized within a few microKelvin by an active temperature controller build-in the FDM bracket supporting the detectors array chip. A constant or slow change of the thermal load on the bracket, caused by mechanical vibrations, only affects the minimum achievable base temperature, and the stability of the detector response is in general guaranteed by the temperature controller. However, an amplitude modulation of the vibrations by relatively fast signals, such as the PT beats at 1.4 Hz and its higher harmonics, could be detected by the TES's before the temperature controller has time to react. As a consequence, an excess noise could be generated in the detector as it was observed in the spectrogram of Fig. 3 and in the noise spectra of Fig. 4. We directly probed this mechanism by exciting with the loudspeaker, at a constant amplitude, one of the vibrational modes of the FDM-probe setup shown in Fig. 9. Once the bath temperature was stabilized again, we modulate the excitation signal amplitude with a slowly varying signal at several amplitude modulation (AM) frequencies, namely, 0.5, 1.78, 2.38, 3.58, 4.47, and 8.7 Hz. The AM signal was directly observed in the pixel noise spectrum up to a frequency of about 10 Hz. The results are shown in Fig. 10. The amplitude of the detected coherent signal follows qualitatively the envelope of the excess low frequency noise of the bolometers shown in Fig. 4.

The sensitivity to mechanical vibration is strongly reduced after suspending the X-ray and the bolometer FDM experiments using the Kevlar structure described in Sec. III. This is best seen in the acoustic scan plots of Fig. 11. In the X-ray FDM setup, the fluctuations of the pixels baseline caused by the excitation of the mechanical modes are reduced by more than a factor of 10 using a single-stage attenuator. The two-stage configuration tested with the bolometer
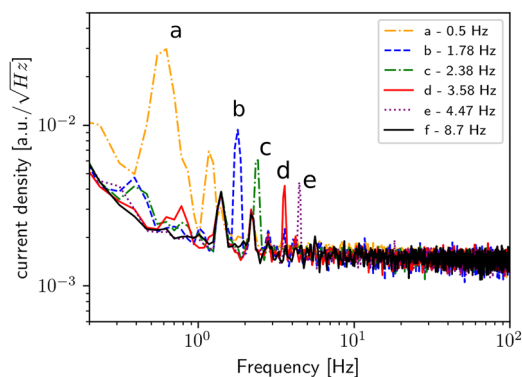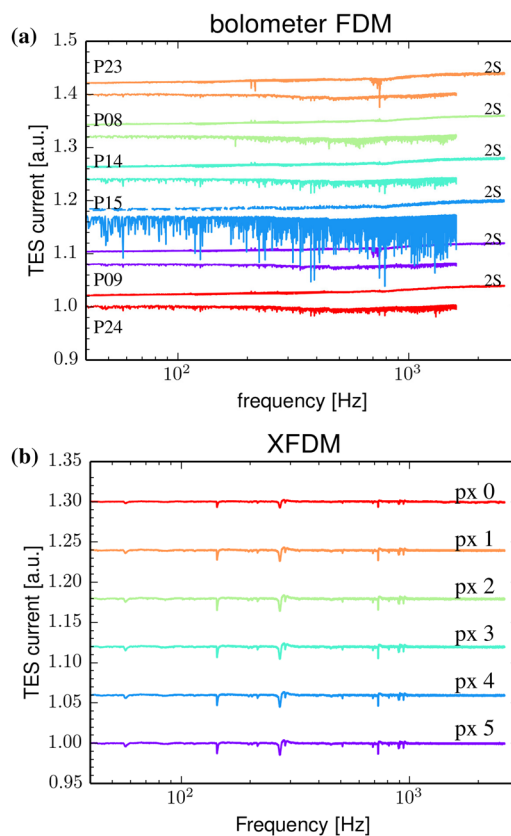

FIG. 11. Baseline signal of the six TES's of the FDM bolometer setup (a) and the X-FDM setup (b) as a function of the excitation frequency of the loudspeaker at the top of the cryostat, after implementing a single-stage acoustic attenuator in both setups. The curved labeled 2S in (a) shows the results of the vibration scan done with the bolometer setup with a two-stage acoustic attenuator.

setup helps to reduce even further the mechanically induced pixel noise.

In Fig. 12, we plot the current noise of four pixels, namely, P09, P15, P23, and P24, from the TES bolometer array described in the Appendix. The TES's were biased at their most sensitive bias point in the transition, and the measurements were done with a single stage and a two-stage attenuation system, respectively. We achieved a noise suppression up to three orders of magnitude at frequencies below 10 Hz. The excess noise at higher frequencies is also reduced. With the two-stage Kevlar-suspended system, we are able to suppress the excess noise generated by the PT down to negligible levels. This is best shown in the current spectral density of Fig. 13, taken with pixel P23 and with the PT switched on and off. In the range from 1 Hz to approximately 20 Hz, the noise floor is dominated by phonon and stray power noise as discussed in our previous studies.[3,4] At frequencies about 20 Hz, the noise increases due to the TES Johnson noise operating in electro-thermal feedback mode.[25] The noise at very low frequencies (below 0.5 Hz), observable in both spectra, is very likely caused by slow bath temperature fluctuations. We exclude here the effect of residual stray light since pixel P15, which has no radiation absorber, showing a similar noise
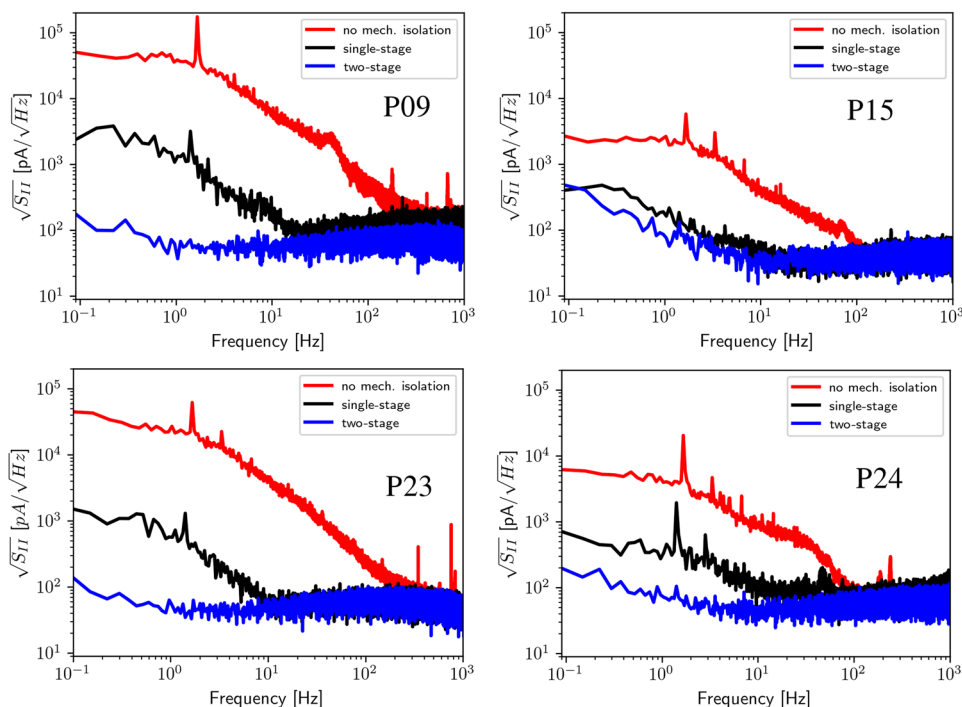

FIG. 10. Coherent signal observed in the FDM-probe X-ray pixel after amplitude modulating, at frequencies of 0.5, 1.78, 2.38, 3.58, and 4.478.7 Hz, the loudspeaker excitation of one of the vibrational modes observed in Fig. 9.

FIG. 12. Current noise of four pixels, namely, $P09$, $P15$, $P23$, and $P24$, from the TES bolometers array. The TES's were biased in the transition, and the measurement was done with the setup directly coupled to the mixing chamber plate (*red*) and after introducing a single stage (*black*) and a two-stage (*blue*) attenuation system.

background at low frequencies. A small contribution from the PT is still observable at 1.4 Hz, which could probably be further reduced by a fine adjustment of the compressor and the PT rotary valve high-pressure lines at room temperature.[12,14]

To gain more insight into the mechanism generating the excess noise in the bolometer detectors, we have measured, simultaneously in FDM mode, the PSD of the six TES's described in Table II. We have looked at correlations in the pixel noise, biasing the detectors in the superconducting and transition states, and before and after
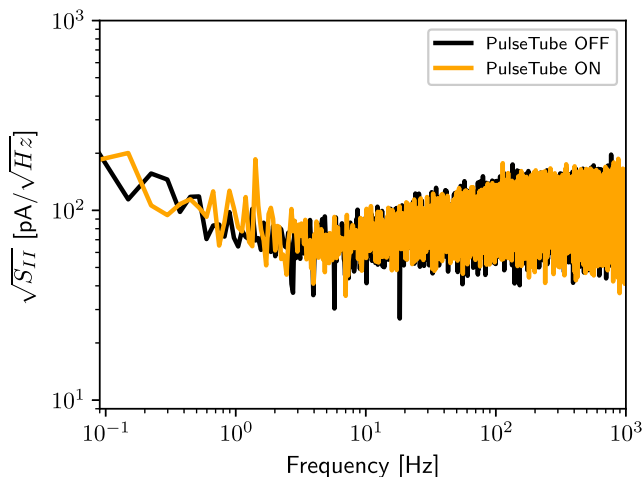

FIG. 13. CSD of one TES bolometer biased in transition and measured with the two-stage Kevlar-suspended system and with the pulse tube temporarily switched off.

implementing the vibration attenuation system. It is useful to visualize the multidimensional data set by scatterplot matrices.[26] The results are shown in Figs. 14–16. The diagonal histograms show the distribution of the PSD for each pixel. In each plot, the dashed lines indicate the mean value and the estimated errors. The off-diagonal plots display the correlation of the power spectral density between each pixel pair. In each figure, we show the averaged PSD of the low frequency side of the spectra ranging from 0 to 2 Hz. In Fig. 16(b), the correlation of the pixel PSD averaged at 25 ± 2 Hz is also shown.

When the FDM bolometer setup is directly mounted on the mixing chamber plate, without attenuation, and the pixels are in the superconducting state [Fig. 14(a)], the noise distribution of each pixel is non-Gaussian and bi-stable behavior is observed, in particular, with pixel P23. A small correlation is measured between the pixel pair P23-P14, P23-P08, and P08-P14, where the pixels are biased at neighboring frequencies of 1.1 MHz, 1.4 MHz and 1.5 MHz, and

TABLE II. Parameters of the TES bolometer array used in the FDM experiment described in the text. Pixels P14 and P15 have no infrared-absorbers and are used to test the darkness of the experimental setup.[3,4] The thermal conductance to the bath of the TES legs is ~30 fW for P14 and P15 and ~60 fW for the other pixels.

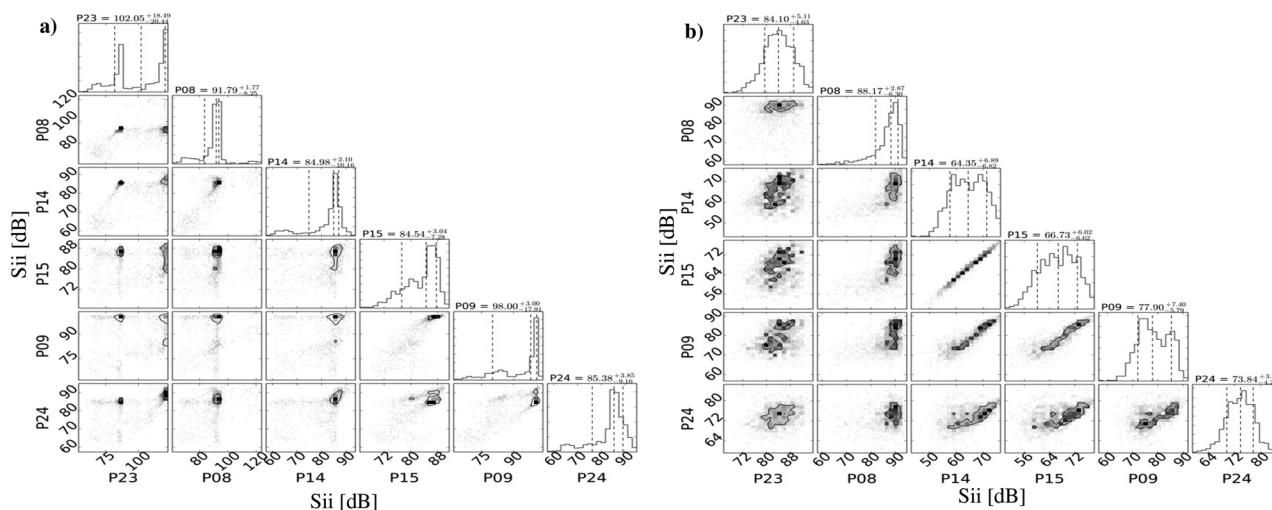| Pixel	LC filter frequency (kHz)	Features
P23	1100	w absorber
P08	1466	w absorber
P14	1579	w/o absorber
P15	2325	w/o absorber
P09	2423	w absorber
P24	2741	w absorber

FIG. 14. Scatter-plot matrices showing the correlation between 5 TES bolometer measured in the superconducting state (a) and in the resistive transition (b). The diagonal histograms show the distribution of the PSD for each pixel. In each plot, the dashed lines indicate the mean value and the estimated errors. The off-diagonal plots display the correlation of the power spectral density between each pixel pair. In each plot, we show the averaged PSD of the low frequency side of the spectra from 0 to 2 Hz.

between the pixel pairs P15-P24, P24-P09 and P15-P09, with the pixels biased at frequencies 2.3 MHz, 2.4 MHz and 2.7 MHz. The PSD correlation has been observed between pixels which are well separated in space, for example pixel P23 and P14, or pixels P24 and P15 (see Fig. 19). The pixels P14 and P15, which shares the same silicon beam in the array, show negligible correlation when they are both in the superconducting state. Only pixels with neighboring bias frequencies show the correlated noise in the superconducting

state, which indicate the presence of electrical cross talk. The cross talk is likely caused by parasitic effects in the FDM readout circuit, for example, the current and voltage leakage caused by the common inductance in the ac bias line and the SQUID input line or the mutual inductance between the high-Q LC filters.

The scenario changes when all the pixels are biased in the transition at about 20%–30% of their normal resistance R_N [Fig. 14(b)]. A strong positive correlation of the PSD is measured between the
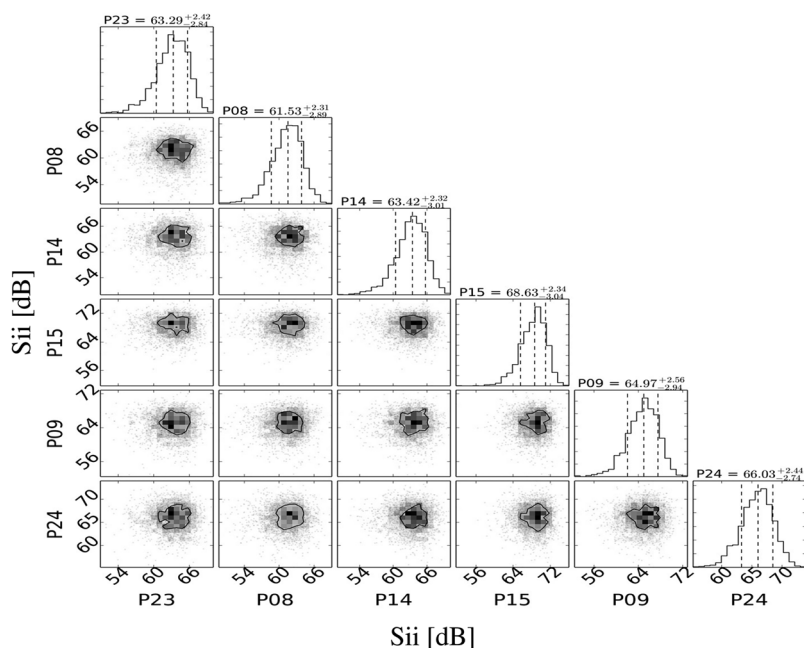

FIG. 15. Scatter-plot matrices showing the correlation between 5 TES bolometers measured in the superconducting state after introducing the two-stage acoustic attenuator described in the text.
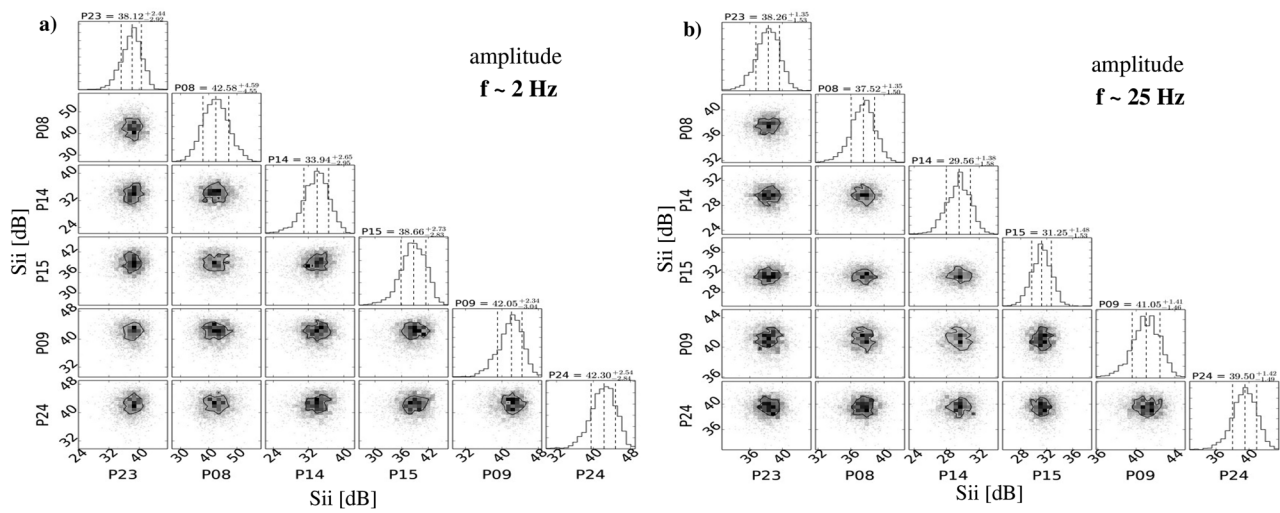
FIG. 16. Scatter-plot matrices showing the correlation between 5 TES bolometers measured at the resistive transition, after introducing the two-stage acoustic attenuator described in the text. In each plot, we show the averaged PSD of the low frequency side of the spectra from 0 to 2 Hz (a) and at 25 ± 2 Hz (b).

pixels P14, P15, and P09. A small correlation is present between these pixels and P24 as well. The noise of the pixels P23 and P08 does not show significant correlation with the other pixels.

The number of pixels measured is too low to draw a solid conclusion on the origin of the observed noise correlation between the pixels biased at the resistive transition. However, we can speculate the following. The silicon chip hosting the bolometer array is mechanically clamped in the middle-top and middle-bottom side of the chip, as shown in Fig. 19(b). The largest displacement occurs very likely at the left and right side of the chip, and at the center of the chip. The pixels showing noise correlation are located at the left side of the array. One possibility is that the fluctuations in the pixels P09, P14, P15, and P24, given their location in the array, are caused by dissipation from the same mechanical vibrational mode of the silicon chip.

The most important fact is, however, that the noise correlation disappears after the implementation of the vibration attenuation system described above. In Figs. 15 and 16, the scatter-plot matrices of the pixel PSD, measured with the bolo-FDM mounted on a single-stage attenuation system, are shown for the TES's in the superconducting and transition states.

In the superconducting state, the pixels do not show the bistable behavior found without the mechanical attenuation, and the distribution of the noise at low frequencies is Gaussian. The noise level measure with attenuation is also about 20–40 dB lower than the noise shown in Fig. 14(b).

Furthermore, with all the TES's in transition, there is no measurable correlation in the pixels current noise, except for a small one at low frequencies between the pixels P14 and P15. The mean value of the distribution of the averaged PSD at 2 Hz for all the measured pixels is about a factor of 2 lower than the one measured without attenuation. There is still a residual low frequency noise, which could explain the observed correlation between P14 and P15, when using a single-stage mechanical isolator. This is consistent with the plots in Fig. 12.

V. CONCLUSION

We have developed an acoustic mechanical attenuator, based on a two-stage mass-spring system, to eliminate the cryocooler-induced low frequency noise observed in low temperature TES-based radiation detectors under development for the instruments of the next generation of infra-red and X-ray space observatories. The acoustic mechanical resonances of the TES pixels, the Si chip, and the Cu bracket supporting the FDM circuits are excited and amplitude modulated by the 1.5 Hz and higher harmonics mechanical displacement generated by the pulse-tube firmly mechanically anchored at the 50 K and 2 K plate of the dilution refrigerator. The acoustic isolator attenuates very efficiently, in all the six degrees of freedom, the mechanical vibrations at frequencies above 100 Hz. The performance of the attenuator has been validated using an array of low-G TES bolometers with an NEP of few $10^{-19} W/\sqrt{Hz}$. The low frequency fluctuations in the current spectral density are reduced by more than three orders of magnitude in several bolometer pixels and made them negligible with respect to the intrinsic noise of the detectors.

ACKNOWLEDGMENTS

APPENDIX: THE FDM SETUPS AND THE DETECTORS

The three setups tested in this work consist of arrays of TES-based detectors readout with the FDM setups under development for the infrared and X-ray instruments SAFARI[15] and X-IFU.[6] The FDM readout of an array of TES microcalorimeters or bolometers is achieved by coupling the sensors to an array of high-Q

superconducting lithographic LC filters,[27] resonating at different frequencies in a typical range from 1 to 5 MHz. The signal from the TES-LC resonator channels is combined and send to the input coil of a very low noise Superconducting QUantum Interference Device (SQUID) array amplifier developed at VTT,[28,29] for the microcalorimeters array FDM setups, and at PTB[30] for the bolometers array setup. As an example, we show in Fig. 17 the FDM bracket assembly used for the bolometer experiment. More details on the X-ray and bolometer FDM setup can be found in Refs. 4, 17, and 31. The electrical connections from the cold stage of the cooler to the SQUID array, and the TES bias circuit elements are achieved by means of NbTi/CuNi superconducting looms of twisted pairs fed through a narrow 10 mm long channel filled with carbon loaded epoxy. The same superconducting looms are used to bring the signal from 30 mK to 3 K. Above 3 K, a combination of CuNi and Cu looms of twisted pairs is used. Each loom is thermally anchored at any of the cooler temperature stages using gold plated copper plates filled with stycast epoxy. The signal is read out at room temperature by FDM electronics developed at SRON.[32] To reduce the

electro-magnetic interferences from the external environment, the external shield of the cryostat has been modified from the original design to form a fully closed Faraday cage in combination with the room temperature electronics.

One of the three FDM experiments, the FDM-probe, is mounted on a 50-mm top-loading probe that can be inserted through a clearshot tube, while the cooler remains at 4 K. The probe is mechanical and thermally clamped at any temperature stages of the cryostat. The probe cold stage fits into a double magnetic shield made of cryoperm and lead, which is fixed on the mixing chamber plate of the DR. A residual uniform magnetic field less than 0.2 μT has been measured at the detector array site inside the shield. The FDM-probe can reach temperature below 50 mK and is used to perform the ac-bias characterization of X-ray TES microcalorimeters.[33] A 3D model of the FDM-probe is shown in Fig. 18. A simple mechanical vibration attenuation has been placed between the FDM bracket and the probe cold stage. It consists of a stack of thin resin rings assembled together using brass bolts. The pulse tube induced oscillations observed in the X-ray detector have been reduced of
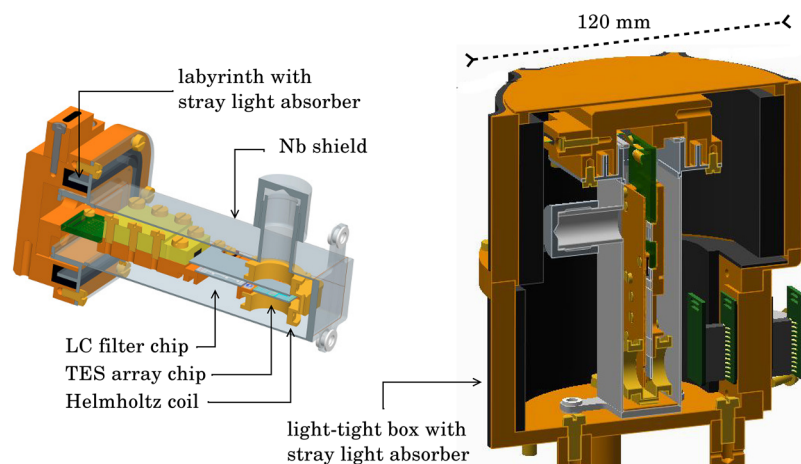

FIG. 17. Cross section of the FDM-setup used to characterize TES-based bolometers. Left: The FDM bracket hosting the superconducting circuit including the SQUID amplifiers, the high-Q LC-filters, and the TES array. The bracket is inserted into a light-tight superconducting Nb shield. Right: The FDM setup in a second light-tight copper housing coated with SiC-loaded black stycast epoxy.
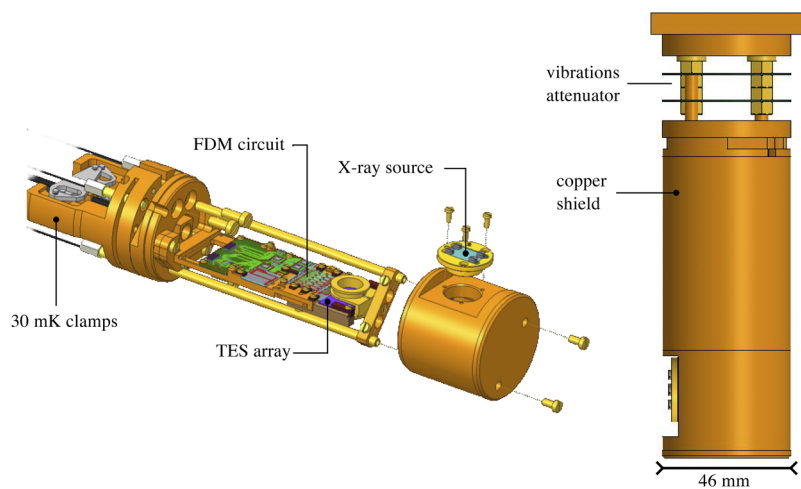

FIG. 18. Schematic of the FDM setup assembled on the 50 mm removable probe. A radioactive Fe^{55} X-ray calibration source is mounted on the copper shield in front of the TES microcalorimeter array. A simple mechanical attenuator (right), made of two thin PCB rings acting as springs, has been placed between the FDM bracket and the plate clamped to the main cooler mixing chamber plate.
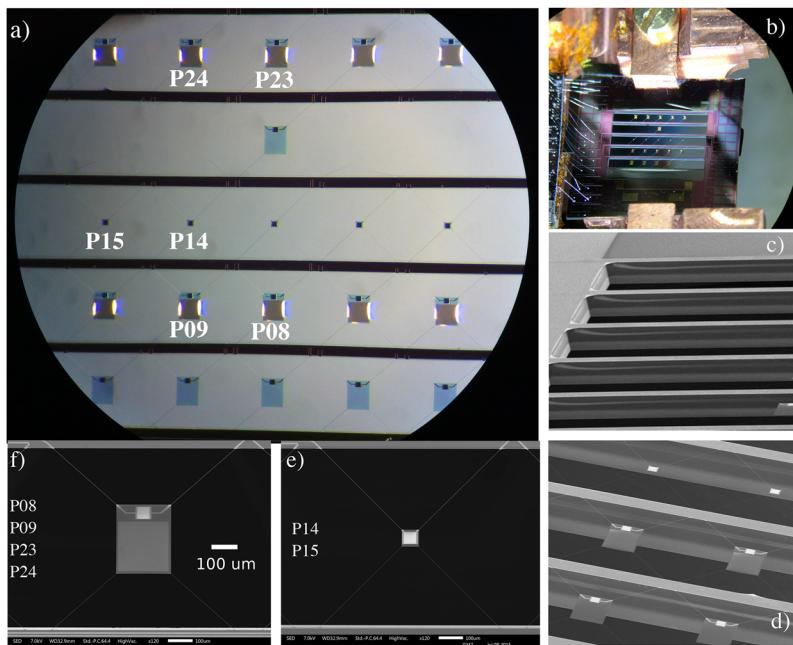
FIG. 19. Pictures of the TES bolometer array used in the acoustic microvibration experiment. (a) Picture of the array center with the measured pixels. (b) Details of the mechanical clamping of the array on the FDM copper bracket. (c) Details of the Si bulks supporting the TES pixels. (d) The long SiN legs and the SiN membrane island hosting the TES's. [(e) and (f)] Pictures of the measured detectors without and with the Ta infra-red radiation absorber.

about a factor of 3 using this simple attenuator. The performance of this attenuator will not be discussed further in the text. The second and third setups, called, respectively, X-FDM and bolo-FDM further in the text, are relatively large and massive and are fixed to the mixing chamber plate of the dilution refrigerator. They are used to read out in FDM mode an array of high energy resolving power X-ray TES-microcalorimeters from NASA-Goddard[6] and an array of ultralow-G TES-bolometers from SRON[3,4]. Both FDM brackets are made of low magnetic impurity copper and host the superconducting and bias circuit components. They are inserted into a light-tight niobium shield to provide both radiation and magnetic shielding. A cryoperm shield was used around the X-FDM setup to attenuate the static magnetic field at the sensor location. A residual uniform magnetic field less than 0.2 μT has been achieved at the detector array site. Details of the X-ray array can be found in Ref. 34. It consists of a 5 mm × 5 mm array of MoAu TES's with Au-Bi absorber deposited on a 0.5 μm thick SiN membrane, etched from a Si chip. The resonant frequencies of the mechanical modes of the Si chip and the membrane are expected to lie above the kilohertz. The bolo-FDM setup was mounted inside a second radiation shield made of copper black-coated with 5% SiC loaded stycast[35,36] in a box-in-box configuration to improve further the light-tightness.[4]

Pictures of the bolometers array and the TES's tested in this work are shown in Fig. 19. The detector array is fabricated at SRON and consists of 50×50 μm^2 TiAu TES's deposited on the thin SiN membrane island and is connected to the Si chip via 4 thin (0.20 μm), narrow (0.5–0.7 μm), and long (340–460 μm) SiN legs. The thermal conductance to the bath has been measured to be 30–60 fW depending on the detector design.

We measured TES bolometers at different bias frequencies with and without radiation absorbers as summarized in Table II.

REFERENCES

[1] P. Roelfsema *et al.*, Proc. SPIE **10698**, 106980A (2018).

[2] D. Barret *et al.*, Proc. SPIE **10699**, 1069901 (2018).

[3] T. Suzuki, P. Khosropanah, M. L. Ridder, R. A. Hijmering, J. R. Gao, H. Akamatsu, L. Gottardi, J. van der Kuur, and B. D. Jackson, J. Low Temp. Phys. **184**, 52 (2016).

[4] P. Khosropanah, T. Suzuki, M. L. Ridder, R. A. Hijmering, H. Akamatsu, L. Gottardi, J. van der Kuur, J. R. Gao, and B. D. Jackson, Proc. SPIE **9914**, 99140B (2016).

[5] S. J. Smith, J. S. Adams, S. R. Bandler, G. L. Betancourt-Martinez, J. A. Chervenak, M. P. Chiao, M. E. Eckart, F. M. Finkbeiner, R. L. Kelley, C. A. Kilbourne, A. R. Miniussi, F. S. Porter, J. E. Sadleir, K. Sakai, N. A. Wakeham, E. J. Wassell, W. Yoon, D. A. Bennett, W. B. Doriese, J. W. Fowler, G. C. Hilton, K. M. Morgan, C. G. Pappas, C. N. Reintsema, D. S. Swetz, J. N. Ullom, K. D. Irwin, H. Akamatsu, L. Gottardi, R. den Hartog, B. D. Jackson, J. van der Kuur, D. Barret, and P. Peille, Proc. SPIE **9905**, 99052H (2016).

[6] H. Akamatsu, L. Gottardi, J. van der Kuur, C. P. de Vries, K. Ravensberg, J. S. Adams, S. R. Bandler, M. P. Bruijn, J. A. Chervenak, C. A. Kilbourne, M. Kiviranta, A. J. van der Linden, B. D. Jackson, and S. J. Smith, Proc. SPIE **9905**, 99055S (2016).

[7] H. Akamatsu, L. Gottardi, J. van der Kuur, C. de Vries, M. P. Bruijn, J. A. Chervenak, M. Kiviranta, A. J. van den Linden, B. D. Jackson, A. Miniussi, K. Sakai, S. J. Smith, and N. A. Wakeham, Proc. SPIE **10699**, 106991N (2018).

[8] A. T. de Waele, J. Low Temp. Phys. **164**, 179 (2011).

[9] A. Chijioke and J. Lawall, Cryogenics **50**, 266 (2010).

[10] M. Pelliccione, A. Sciambi, J. Bartel, A. J. Keller, and D. Goldhaber-Gordon, Rev. Sci. Instrum. **84**, 033703 (2013).

[11] S. Caparrelli, E. Majorana, V. Moscatelli, E. Pascucci, M. Perciballi, P. Puppo, P. Rapagnani, and F. Ricci, Rev. Sci. Instrum. **77**, 095102 (2006).

[12] A. M. J. den Haan, G. H. C. J. Wijts, F. Galli, O. Usenko, G. J. C. van Baarle, D. J. van der Zalm, and T. H. Oosterkamp, Rev. Sci. Instrum. **85**, 035112 (2014).

[13] E. Olivieri, J. Billard, M. D. Jesus, A. Juillard, and A. Leder, Nucl. Instrum. Methods Phys. Res., Sect. A **858**, 73 (2017).

[14] R. Kalra, A. Laucht, J. P. Dehollain, D. Bar, S. Freer, S. Simmons, J. T. Muhonen, and A. Morello, Rev. Sci. Instrum. **87**, 073905 (2016).

[15]P. Roelfsema, M. Giard, F. Najarro, K. Wafelbakker, W. Jellema, B. Jackson, B. Sibthorpe, M. Audard, Y. Doi, A. di Giorgio et al., Proc. SPIE **9143**, 91431K (2014).

[16]J. Wijker, *Mechanical Vibrations in Spacecraft Design* (Springer-Verlag, 2004).

[17]L. Gottardi, H. Akamatsu, M. Bruijn, J.-R. Gao, R. den Hartog, R. Hijmering, H. Hoevers, P. Khosropanah, P. de Korte, J. van der Kuur, A. van der Linden, M. Lindeman, and M. Ridder, Proc. SPIE **8453**, 845333 (2012).

[18]E. Coccia, Rev. Sci. Instrum. **53**, 148 (1982).

[19]H. W. Chan, J. C. Long, and J. C. Price, Rev. Sci. Instrum. **70**, 2742 (1999).

[20]T. L. Aldcroft, P. F. Michelson, R. C. Taber, and F. A. McLoughlin, Rev. Sci. Instrum. **63**, 3815 (1992).

[21]A. de Waard, Y. Benzaim, G. Frossati, L. Gottardi, H. van der Mark, J. Flokstra, M. Podt, M. Bassan, Y. Minenkov, A. Moleti, A. Rocchi, V. Fafone, and G. Pallottino, Classical Quantum Gravity **22**, S215 (2005).

[22]M. Bignotto, M. Bonaldi, M. Cerdonio, L. Conti, F. Penasa, G. A. Prodi, G. Soranzo, L. Taffarello, and J.-P. Zendri, Rev. Sci. Instrum. **76**, 084502 (2005).

[23]M. Saraceni, M. Bonaldi, L. Castellani, L. Conti, A. B. Gounda, S. Longo, and M. Pegoraro, Rev. Sci. Instrum. **81**, 035115 (2010).

[24]L. Duband, L. Hui, and A. Lange, Cryogenics **33**, 643 (1993).

[25]K. D. Irwin and G. C. Hilton, *Cryogenic Particle Detection* (Springer-Verlag, 2005), pp. 63–149.

[26]D. Foreman-Mackey, J. Open Source Software **1**, 24 (2016).

[27]M. P. Bruijn, L. Gottardi, R. H. den Hartog, J. van der Kuur, A. J. van der Linden, and B. D. Jackson, J. Low Temp. Phys. **176**, 421 (2014).

[28]M. Kiviranta, L. Grönberg, N. Beev, and J. van der Kuur, J. Phys.: Conf. Ser. **507**, 042017 (2014).

[29]L. Gottardi, M. Kiviranta, J. van der Kuur, H. Akamatsu, M. P. Bruijn, and R. den Hartog, IEEE Trans. Appl. Supercond. **25**, 1 (2015).

[30]D. Drung, J. Beyer, M. Peters, J.-H. Storm, and T. Schurig, IEEE Trans. Appl. Supercond. **19**, 772 (2009).

[31]L. Gottardi, J. Adams, C. Bailey, S. Bandler, M. Bruijn, J. Chervenak, M. Eckart, F. Finkbeiner, R. den Hartog, H. Hoevers, R. Kelley, C. Kilbourne, P. de Korte, J. van der Kuur, M. Lindeman, F. Porter, J. Sadlier, and S. Smith, J. Low Temp. Phys. **167**, 214 (2012).

[32]R. den Hartog, M. Audley, J. Beyer, D. Boersma, M. Bruijn, L. Gottardi, H. Hoevers, R. Hou, G. Keizer, P. Khosropanah, M. Kiviranta, P. de Korte, J. van der Kuur, B.-J. van Leeuwen, A. Nieuwenhuizen, and P. van Winden, J. Low Temp. Phys. **167**, 652 (2012).

[33]L. Gottardi, H. Akamatsu, J. van der Kuur, S. J. Smith, A. Kozorezov, and J. Chervenak, IEEE Trans. Appl. Supercond. **27**, 1 (2017).

[34]N. Iyomoto, S. R. Bandler, R. P. Brekosky, A.-D. Brown, J. A. Chervenak, E. Figueroa-Feliciano, F. M. Finkbeiner, R. L. Kelley, C. A. Kilbourne, F. S. Porter, J. E. Sadleir, and S. J. Smith, Appl. Phys. Lett. **92**, 13508 (2008).

[35]M. C. Diez, T. O. Klaasen, K. Smorenburg, V. Kirschner, and K. J. Wildeman, Proc. SPIE **4013**, 129 (2000).

[36]P. Hargrave, Nucl. Instrum. Methods Phys. Res., Sect. A **444**, 427 (2000).